Heliyon 10 (2024) e40157

Contents lists available at ScienceDirect

Heliyon

journal homepage: www.cell.com/heliyon

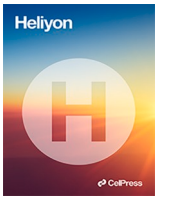

Research article

Role of perovskite non-stoichiometry on catalytic oxygen dark activation for the removal of azo dyes from wastewater

Sadia Manzoor, Qasim Imtiaz *

Department of Chemistry and Chemical Engineering, Lahore University of Management Sciences, DHA, Lahore Cantt, 54792, Lahore, Pakistan

ARTICLE INFO

Keywords:
Azo dyes
Advanced oxidation processes
O_2 dark activation
Catalysis
Perovskites
Non-stoichiometry
$SrFeO_3$

ABSTRACT

Effluents of the dying and printing industries are a significant contributor to water pollution. Since synthetic dyes are primarily resistant to natural degradation, they remain in water bodies for an exceptionally long time if discharged untreated. Oxygen dark activation is a promising candidate for the degradation of azo dyes as it does not require the use of additional reagents or even the presence of light. It is an advanced catalytic oxidation process that converts oxygen dissolved in wastewater into reactive oxygen species, which subsequently break down dye molecules. The role of the catalyst is to accelerate the process by acting as a bridge for the electron transfer between the dye molecules and adsorbed oxygen. It has been reported that the textural and structural properties of the catalyst play a key role in generating reactive oxygen species. In this work, we synthesized, characterized, and evaluated a series of strontium-based perovskite oxides for the catalytic degradation of azo dyes under dark conditions. The degradation of different dyes was studied in a batch reactor under various conditions, and the reaction progress was monitored by UV–vis absorption spectroscopy. The results showed that the degradation of azo dye was faster when the azo bond was weakened by either electron-withdrawing groups or due to the formation of a stable hydrazone structure. To evaluate the effect of structural defects on the oxygen dark activation process, cation non-stoichiometry was separately introduced in the parent perovskite $SrFeO_3$ at both A and B sites. Under identical reaction conditions, the degradation efficiency of A-site deficient perovskite $Sr_{0.90}FeO_3$ (94 %) and B-site deficient $SrFe_{0.80}O_3$ (95 %) was higher than the stoichiometric perovskite $SrFeO_3$ (46 %). These results demonstrate that cation deficiency in the $SrFeO_3$ structure strongly favors the catalytic degradation of azo dyes *via* oxygen dark activation.

1. Introduction

The textile manufacturing sector has been a cornerstone of the global economy for centuries, weaving a tapestry of cultural, economic, and technological significance. The textile industry experienced remarkable growth and transformation in recent decades due to a rising population, increasing disposable incomes, and changing lifestyles [1]. Unfortunately, this expansion has created a complex fabric of global environmental challenges, particularly in the form of textile wastewater, which accounts for over 20 % of total industrial wastewater [2]. The dyeing and finishing processes in textile manufacturing consume a large amount of water and produce effluents containing different dyes, heavy metals, and other pollutants. These dyes and chemicals give textile effluents their

* Corresponding author.
E-mail address: qasim.imtiaz@lums.edu.pk (Q. Imtiaz).

https://doi.org/10.1016/j.heliyon.2024.e40157
Received 17 August 2024; Received in revised form 18 October 2024; Accepted 4 November 2024
Available online 10 November 2024

undesirable visual appearance and have the potential to contaminate the nearby soil, sediment, and groundwater due to their toxicity [3]. Many of these dyes are known to cause neurological and reproductive health issues in humans and aquatic species [4]. Consequently, the effluents can only be reused in other textile processes or discharged to a receiving water body after appropriate treatment.

The textile sector currently uses about 10,000 different types of synthetic dyes [5]. These dyes can be categorized into different classes based on their mode of application (e.g., basic, direct, disperse, reactive, and vat dyeing) or chemical structure (e.g., anthraquinone, azo, sulfur, triarylmethane, phthalocyanine, etc.) [1]. In terms of number and production volume, azo dyes comprise 60–70 % of all organic dyes produced worldwide, making them the most important class of synthetic dyes. [6] The azo compounds contain one or more azo groups $-N=N-$ connecting two organic functional groups, one of which is usually an aromatic nucleus (see Fig. 1). The chemical structure of azo compounds makes them nonbiodegradable and resistant to temperature, light, and oxidizing agents, even at low concentrations. Owing to these harmful impacts, several azo dyes have been banned since the mid-1990s, and strict legislation has been enacted to regulate their use [7]. As a result, the removal of azo dyes from textile effluents by conventional wastewater treatment processes is very challenging [8,9]. Several physical (e.g., adsorption [10,11], filtration [12], flocculation [13], reverse osmosis [14], etc.), biological [15] and chemical (advanced oxidation [16] and chemical oxidation [17]) processes have been developed to treat textile wastewater. Although the physical methods are simple and effective, they mainly transfer dyes from one phase to another, generating toxic sludge [18]. Biological processes for the treatment of textile wastewater are environmentally friendly and economical but, at the same time, more time-consuming due to the resistance of aromatic rings to biological degradation [19]. On the other hand, advanced oxidation processes (AOPs) have emerged as more effective and versatile alternatives for treating textile wastewater because of the complete mineralization of synthetic dyes [20]. In AOPs, highly reactive oxidizing species (ROS) (e.g., hydroxyl radicals, hydroperoxyl radicals, sulfate radicals, *etc.*) involved in decomposing organic pollutants into less harmful products like mineral acids, carbon dioxide, and water are produced *in-situ* [21]. Different AOPs, such as the Fenton process (H_2O_2/Fe^{2+}) [22], photo-Fenton process (H_2O_2/Fe^{2+}/UV) [23], photocatalysis [24], ozonation, and oxygen dark activation, have been reported for the treatment of textile effluents [25]. These processes differ in the mechanism through which ROS are produced.

Among different AOPs, the oxygen (O_2) dark activation method uses a catalyst to convert the O_2 dissolved in water into hydroxyl radicals, thus eliminating the need for any additional oxidizing agent or illumination to generate ROS. Besegatto et al. [26] proposed that pollutant molecules initially adsorb onto the catalyst surface, where they convert into cations by transferring electrons to the catalyst. The catalyst then passes those electrons to oxygen molecules, which undergo a series of reactions to produce different ROS. These ROS finally break down the pollutant cations. The reaction mechanism proposed by Besegatto et al. [26] is as follows:

$$(R_1 - N = N - R_2)_{aq} \overset{\text{catalyst}}{\rightarrow} (R_1 - N = N - R_2)_{ad} \quad (1)$$

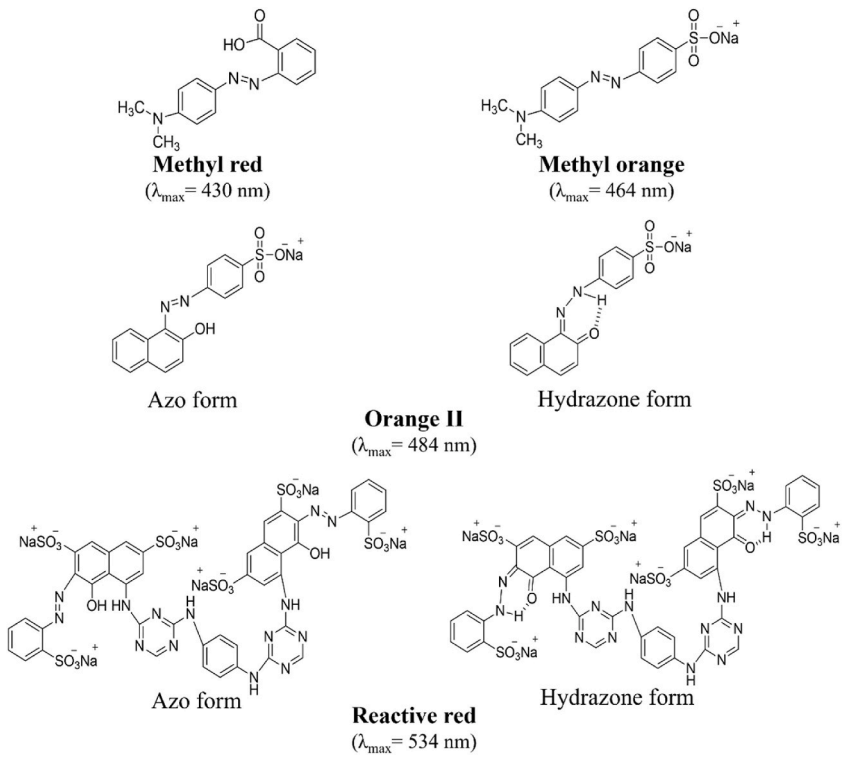

Fig. 1. Chemical structures of azo dyes used in this work.

$$(R_1 - N = N - R_2)_{ad} \overset{\text{catalyst}}{\rightarrow} (R_1 - N = N - R_2)^{+}_{ad} + e^{-} \quad (2)$$

$$e^{-} + O_2 \rightarrow O_2^{-\bullet} \quad (3)$$

$$O_2^{-\bullet} + H^{+} \longleftrightarrow HO_2^{\bullet} \quad (4)$$

$$2HO_2^{\bullet} \rightarrow H_2O_2 + O_2 \quad (5)$$

$$H_2O_2 + e^{-} \rightarrow OH^{\cdot} + OH^{-} \quad (6)$$

$$OH^{\cdot} + (R_1 - N = N - R_2)^{+}_{ad} \rightarrow R_1 - N + (N - R_2)^{+} \quad (7)$$

$$OH^{\cdot} + (N - R_2)^{+} \overset{\text{catalyst}}{\rightarrow} R_3 - N + R_4 + CO_2 \quad (8)$$

The mechanistic study of Besegatto et al. [26] revealed that the contact between the dye molecule and catalyst is the rate-limiting step for O_2 dark activation. The radical trapping experiments of Chen et al. [27] also confirmed the formation of different ROS during the oxidative degradation of Orange II in dark conditions. These and several other studies suggest that a catalyst that activates oxygen under dark conditions should possess favorable energetics for (i) adsorbing dissolved O_2 and (ii) electron transfer to O_2.[28 29] Different materials, such as oxides and complexes of transition metals [28] and perovskite oxides [25], have shown promising activity for the degradation of azo dyes *via* the oxygen-dark activation process. Among these catalysts, perovskite-type oxides offer the most flexibility in terms of selection/tuning of elements at A and B sites, oxygen vacancies, and doping of other metals at A and/or B sites [29]. However, the main disadvantage of using perovskites for the oxygen dark activation process is their low surface area, thus limiting contact with the dye molecules [30].

Perovskite oxides require a higher calcination temperature (700 °C – 1000 °C) during their synthesis, significantly reducing their surface area. Several approaches have been reported in the literature to increase their surface area and, thus, the interaction between the perovskite-type catalyst and dye molecules. For example, Leiw et al. [30] used a ball milling process to reduce the size of $SrFeO_3$ perovskite particles to less than 500 nm, increasing surface area. On the other hand, Wu et al. [31] deposited $AgBiO_3$ perovskite on g-C_3N_4 support to increase the surface area for the adsorption of organic pollutants, which in turn increased the degradation of methyl orange from 83.7 % to 95 %. Doping at the A- or B-site of the perovskite-type oxides is another commonly used approach to increase the activity of parent perovskite [26,32]. Tummino et al. [33] doped 15 mol. % cerium at the A-site of $SrFeO_3$ to achieve a 95 % degradation of Orange II at 80 °C under dark conditions. The catalytic properties of perovskites can also be tuned by adjusting the cation's content, either with deficiencies or excesses. The resulting non-stoichiometry creates structural defects that generate oxygen vacancies to stabilize the perovskite lattice [34]. The use of non-stoichiometric modification in perovskite oxides has been explored for AOPs like peroxymonosulfate (PMS) activation for wastewater treatment [35] and other applications, such as energy conversion and storage [36], but not for oxygen dark activation [37,38].

This work evaluates the influence of non-stoichiometry at the A- and B-site of perovskite on oxygen dark activation for removing azo dyes from wastewater. For this, we used $SrFeO_3$ as a model catalyst and employed a sol-gel method to introduce metal deficiencies at the Sr- and Fe-sites separately. Detailed characterization and catalytic evaluation of the synthesized perovskites were used to explore the non-stoichiometry-activity relationship. Finally, we used different azo dyes to shed light on the role of structural parameters, such as substituent group and steric hindrance, in catalytic degradation.

2. Materials and method

2.1. Catalyst synthesis

All reagents were purchased from Daejung Chemicals & Metals and used as received. Stoichiometric $SrFeO_3$, and A- and B-site deficient perovskite series with general formula Sr_xFeO_3 (where x = 0.95, 0.90, 0.85 or 0.80) and $SrFe_yO_3$ (y = 0.95, 0.90, 0.85, 0.80 or 0.70) were synthesized using the modified Pichini method [39]. In a typical synthesis, required amounts of the metal nitrate precursors were first dissolved in deionized water under continuous stirring, followed by the addition of citric acid. The reaction mixture was heated to 50 °C, and ethylene glycol was added dropwise at 50 °C. The ratio of metal cations: citric acid: ethylene glycol was kept at 1: 2.5: 3.75 in all synthesis. The temperature of the reaction mixture was subsequently increased to 80 °C and maintained at that temperature until a gel formed. The resulting gel was dried overnight at 130 °C and calcined at different temperatures for 3 h to obtain the perovskite phase. Finally, the calcined material was sieved in the size range 53–74 μm.

2.2. Characterization

Powder X-ray diffraction (XRD) was used to identify the crystalline phases in the calcined samples. X-ray diffractograms were recorded on a Bruker D2 Phaser diffractometer in the 2θ range 20° – 80° using Cu K_α radiations (λ = 1.5406 Å). The diffractometer was operated at 30 kV and 10 mA. The crystallite size was estimated using the Scherrer equation [40]. The surface morphology of calcined samples was imaged with a scanning electron microscope (Nova NanoSEM 450 FE-SEM), and the average particle size was estimated using ImageJ software [41]. N_2 adsorption isotherms were acquired at −196 °C on a Quantachrome® ASiQwin™ surface analyzer to

determine the surface area of the calcined perovskites. Before analysis, the catalysts were degassed for 3 h at 300 °C. The Brunauer–Emmett–Teller (BET) method was used to estimate the surface area [36]. Zeta potential (ζ, mV) was measured to determine the surface charge of perovskite oxides in aqueous solution at different pH values (i.e., 2, 6, 10) and room temperature (25 °C) with Malvern Zetasizer Nano. For this purpose, approximately 1 mg of catalyst was dispersed in 40 mL of deionized water and sonicated for 15 min to homogenize the solution/dispersion of particles. 1 M HCl or NaOH solution was used to achieve the desired pH value. The final value of zeta potential was obtained by averaging ten measurements.

2.3. Catalytic activity

The degradation activity of the synthesized catalysts was evaluated at different temperatures and pH values in a 250 mL batch reactor. In a typical experiment, 100 mL of 10 mgL^{-1} dye solution was heated to the desired reaction temperature, and subsequently, 500 mgL^{-1} of catalyst was dispersed in the solution under continuous magnetic stirring. The dye oxidation reaction was carried out in the dark under a blanket of air. To track the changes in the dye concentration with time, 1 mL of the reaction mixture was withdrawn with the help of a syringe from the reaction vessel at designated intervals, centrifuged at 14000 rpm, and analyzed using an Agilent Cary 60 UV–vis spectrophotometer. Prior to analysis, the spectrophotometer was calibrated using different standard solutions of azo dyes. A blank degradation experiment was always performed without the catalyst under identical reaction conditions to check the possibility of self-degradation. The percent degradation was calculated according to equation (9).

$$\%\ \text{degradation} = \left(1 - \frac{C_t}{C_0}\right) \times 100 \tag{9}$$

where, C_t is the concentration (mgL^{-1}) of dye in the solution at time t, and C_0 is the initial concentration of the dye solution. To ensure reproducibility, all experiments were repeated thrice.

3. Results and discussion

3.1. Characterization of stoichiometric $SrFeO_3$ catalysts

The powder XRD patterns of the $SrFeO_3$ catalysts calcined in the temperature range 200–800 °C for 3 h are shown in Fig. 2. As expected, no crystalline phase was identified in the x-ray diffractogram of the material calcined at 200 °C. At 400 °C, broad peaks corresponding to the $SrCO_3$ phase were present, likely formed by the reaction between CO_2 released from the decomposition of organic matter and SrO [42]. The XRD pattern of the catalyst prepared at 600 °C confirmed the formation of a cubic $SrFeO_3$ phase with an average crystallite size of 18 nm (see Table 1), as estimated using the Scherrer equation. This diffractogram also showed that a small amount of $SrCO_3$ remained in the material calcined at 600 °C. To minimize the amount of $SrCO_3$ formed during calcination, we synthesized another catalyst at 600 °C using a temperature ramp rate of 2 °C/min. Our working hypothesis was that a slower heating rate would result in a slow combustion of organic matter, lowering the local partial pressure of CO_2 released. A reduced partial pressure of CO_2 will decrease the thermodynamic driving force for the formation of the $SrCO_3$ phase. The X-ray diffractograms shown in Fig. S1 indeed confirm that $SrCO_3$ was not formed when the heating rate was lowered from 10 °C/min to 2 °C/min.

Since a higher temperature favors the decomposition of $SrCO_3$ to SrO [43], the diffractograms of the catalysts calcined at 700 °C and 800 °C contained peaks corresponding to the cubic $SrFeO_3$ phase only. The average crystallite size of $SrFeO_3$ prepared at 700 °C and 800 °C was 21 nm and 23 nm, respectively (Table 1). An increase in crystallite size with calcination temperature is expected as

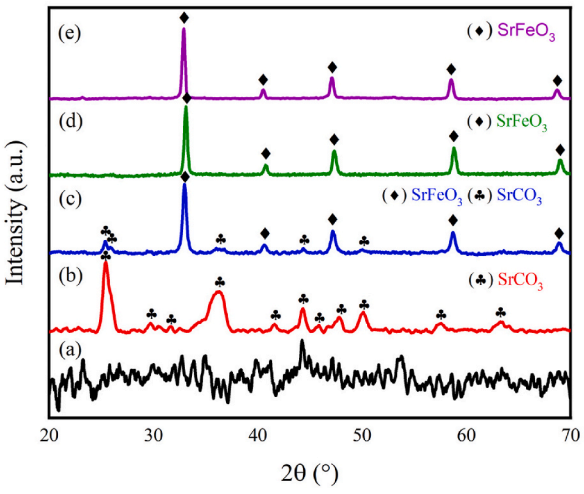

Fig. 2. X-ray diffractograms of $SrFeO_3$ catalysts calcined at (a) 200 °C, (b) 400 °C, (c) 600 °C, (d) 700 °C and (e) 800 °C.

Table 1
Average crystallite size and BET surface area of stoichiometric perovskite catalysts calcined at different temperatures.

Catalyst	Calcination condition	Average crystallite size [nm]	BET surface area [m^2/g]
$SrFeO_3$	600 °C (10 °C/min)	18	23
	600 °C (02 °C/min)	18	18
	700 °C (10 °C/min)	21	11
	800 °C (10 °C/min)	23	10

higher temperature promotes agglomeration and collapse of the microporous structure [44]. Consequently, the surface area of catalysts decreases with increased calcination temperature and time. Table 1 shows that the BET surface area of $SrFeO_3$ calcined at 600 °C for 3 h at a rate of 10 °C/min was the highest at 23 m^2/g. When we calcined the same material at a lower heating rate of 2 °C/min, its surface area decreased to 18 m^2/g. This is most likely due to increased ramp time from ~58 min to ~290 min when the heating rate is reduced. Further increases in calcination temperature to 700 °C and 800 °C decreased the surface area of $SrFeO_3$ to 11 m^2/g and 10 m^2/g, respectively. This decrease is associated with an increase in average crystallite size and aligns with the previous observation of Kucharczyk et al. [45].

The morphology of the samples calcined in the temperature range 600–800 °C was imaged using a high-resolution scanning electron microscope. The surface of the stoichiometric catalyst calcined at 600 °C (see Fig. 3(a)) comprised irregularly shaped particles fused to form a large island. The islands merged into each other to form a dense structure with some visible cracks. The irregularly shaped particles had a size distribution of 68 ± 15 nm. It can be seen from Fig. 3(b) and (c) that calcination at 700 °C and 800 °C led to an increase in the particle size and the formation of even denser surfaces due to enhanced agglomeration. The particle size distribution was calculated to be 163 ± 27 nm and 450 ± 121 nm at 700 °C and 800 °C, respectively. Scanning electron micrograph of the sample calcined at 600 °C at a heating rate of 2 °C/min is shown in Fig. S2. It can be seen from Fig. S2 that a slow heating rate resulted in a coral reef-like surface morphology comprising particles with an average size of 37 nm ± 7 nm, which is almost half compared to the catalyst calcined at a heating rate of 10 °C/min. Comparing the SEM images in Fig. 3(a) and S2, it is evident that the heating rate significantly affects the particle size and surface morphology of perovskites.

3.2. Role of structural parameters of dye in catalytic degradation

Fig. 4(a) plots the catalytic degradation of four different azo dyes, *viz.* methyl red, methyl orange, orange II, and reactive red, at 60 °C in the presence of stoichiometric $SrFeO_3$ calcined at 600 °C. On the other hand, Fig. 4(b) shows a correlation between catalytic degradation and λ_{max} value of the dye molecules used in this work. The activity data in Fig. 4 reveals that the degradation of dyes depends strongly on the strength of the azo bond and the chemical nature of the substituent groups. Among the four azo dyes used in this work, methyl red showed only 13 % degradation after 30 min at 60 °C under dark conditions. As shown in Fig. 1, methyl red has a carboxylic acid group attached at the ortho position with respect to the azo group, which sterically hinders the azo bond, making its cleavage difficult. Unlike methyl red, methyl orange has no functional group in the close vicinity of the azo bond. Consequently, its degradation was around 67 % after 30 min. The same trend has previously been reported by Goncalves et al. [46], who showed that dyes containing the sulphonic acid group (e.g., methyl orange) degrade faster because of the strong electron-withdrawing effect [47].

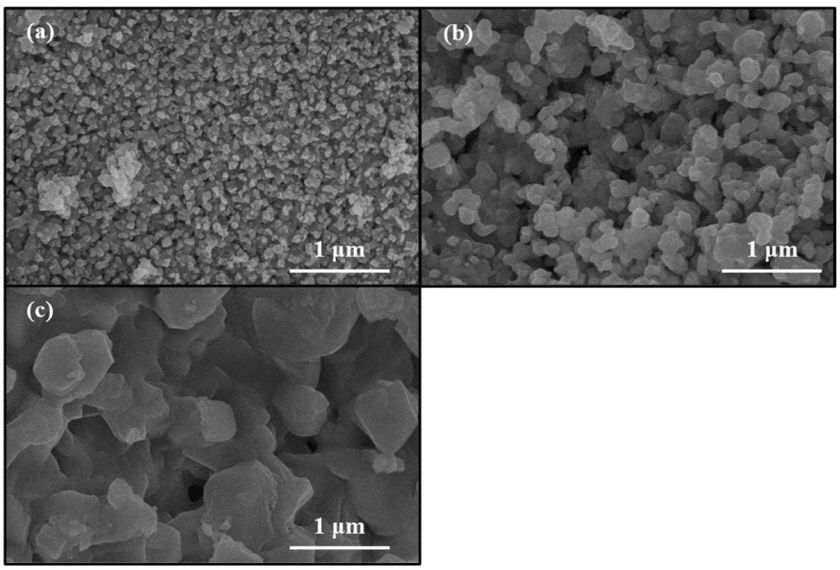

Fig. 3. Scanning electron micrographs of $SrFeO_3$ catalysts calcined at (a) 600 °C, (b) 700 °C and (c) 800 °C.

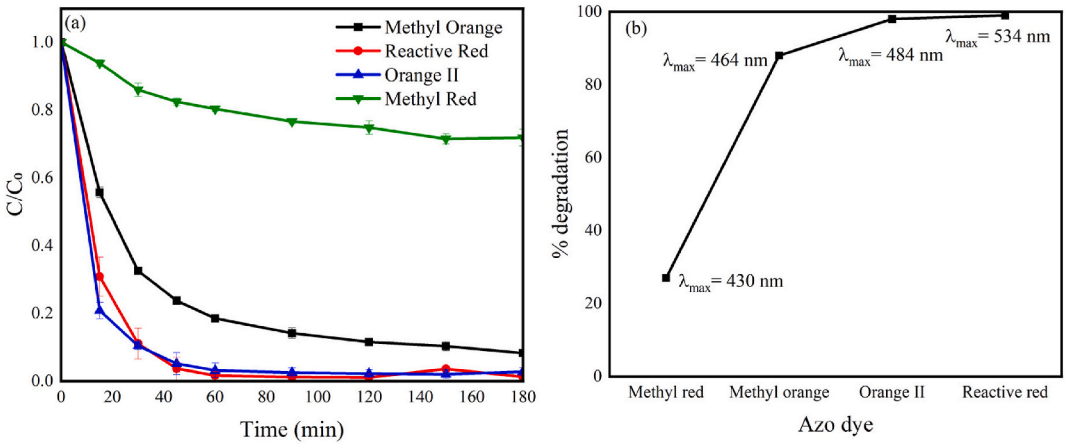

Fig. 4. (a) Catalytic degradation of methyl red, methyl orange, orange II, and reactive red in the presence of $SrFeO_3$ calcined at 600 °C. (b) Percent degradation at 120 min by $SrFeO_3$ calcined at 600 °C as a function of the dye molecule. Reaction conditions: $C_o = 10$ mgL^{-1}, catalyst amount = 500 mgL^{-1}, T = 60 °C, in the dark. (For interpretation of the references to colour in this figure legend, the reader is referred to the Web version of this article.)

On the other hand, the dyes with the carboxylic acid group (e.g., methyl red) are challenging to degrade owing to the higher electron density of the carboxylic group present at the ortho position to the azo bond. Compared to methyl orange, orange II has a hydroxyl group in conjugation with the azo bond and exists in two tautomeric forms, *viz.* azo and hydrazone. In an aqueous solution, the hydrazone form is more favored, which weakens the azo bond by the intramolecular hydrogen bonding, thereby facilitating its breakdown [48]. As a result, orange II dye showed a 90 % decrease in its original concentration after 30 min, as shown in Fig. 4(a). Such intramolecular hydrogen bonding is not possible in methyl orange, as there is no proton-donating group near the azo bond. Surprisingly, the catalytic degradation of reactive red, a diazo dye, was almost comparable with Orange II. Owing to its bulky molecular structure, we expected a low degradation of reactive red compared to mono-azo dyes used in this study [49]. However, we speculate that the hydroxyl group present at the ortho position with respect to the azo bond weakens –N=N– bonds due to the possible intramolecular hydrogen bonding. Fig. 4(b) shows that the dye molecules with lower λ_{max} values were more resistant to catalytic degradation under the reaction conditions used in this study. On the other hand, breaking azo dyes with higher λ_{max} values was relatively easier. Since methyl orange did not degrade completely in 3 h, we selected it for further activity tests using non-stoichiometric perovskites.

3.3. *Effect of temperature and pH on O_2 dark activation*

The effect of the reaction temperature on the O_2 dark activation was studied by comparing the catalytic degradation of methyl

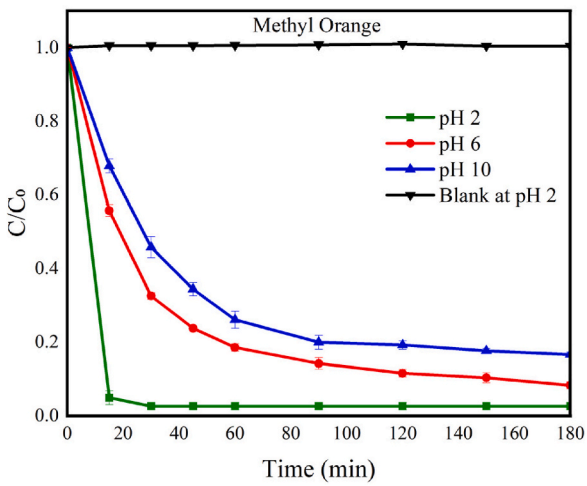

Fig. 5. Catalytic degradation of methyl orange at 60 °C in the presence of $SrFeO_3$ (calcined at 600 °C) at three different pH values. Reaction conditions: $C_o = 10$ mgL^{-1}, catalyst amount = 500 mgL^{-1}, pH = 2, 6 and 10, T = 60 °C, in the dark. (For interpretation of the references to colour in this figure legend, the reader is referred to the Web version of this article.)

orange at 30 °C and 60 °C. The UV–vis spectra collected during the degradation of the methyl orange solution at 60 °C show that the characteristic peak of azo bond at 464 nm decreases with time, see Fig. S3(a). Simultaneously, a peak at 344 nm appears, which most likely corresponds to degradation products. Now, it can be seen from Fig. S3(b) that lowering the temperature of the reaction mixture from 60 °C to 30 °C decreased the (apparent) rate of degradation of methyl orange from 0.022/min to 0.005/min. Consequently, only ~16 % degradation of methyl orange was achieved after 30 min at 30 °C compared to ~67 % at 60 °C. As mentioned in the introduction, the contact between the dye molecules and the catalyst surface is the first and the rate-limiting step in the O_2 dark activation process [26]. We speculate that lowering the reaction temperature decreases the kinetic energy of dye molecules in solution, reducing their collisions with the catalyst particles [50]. Thus, the apparent rate of degradation decreases with reaction temperature. Since adsorption is thermodynamically favorable at lower temperatures, these results confirm that $SrFeO_3$ perovskite breaks down dye molecules by O_2 dark activation instead of simply adsorbing them on its surface.

To investigate the role of solution pH in the activation of O_2 under dark conditions, catalytic degradation of methyl orange was carried out at pH = 2 and 10 at 60 °C. A few drops of 1 M HCl and 1 M NaOH solutions were used to adjust the pH of the dye solution to 2 and 10, respectively. Fig. 5 indicates that a lower pH value favored the catalytic degradation of methyl orange by $SrFeO_3$. At pH 2, almost all dye molecules were cleaved within the first 15 min at an apparent reaction rate of 0.064/min. However, the % degradation after 15 min decreased to 67 % and 30 % at pH 6 and 10, respectively. Moreover, the apparent degradation rate also decreased and was calculated to be 0.029/min and 0.020/min at pH 6 and 10, respectively. Blank experiments under identical conditions confirmed no self-degradation of methyl orange in the acidic or basic solutions. Zeta potential measurements showed that at pH = 2, the catalyst's surface had a positive charge of +15 mV. Therefore, under acidic conditions, there is an increase in electrostatic attraction between the catalyst's surface and anionic dye molecules. The enhanced interaction greatly facilitates dye degradation. On the other hand, in the basic medium, the surface charge was measured to be −38 mV at pH = 10. The negatively charged surface of the catalyst repels the anionic dye molecules, and thus, the catalytic activity of the catalyst decreases as the pH of the reaction medium increases. These results agree with the previous report of Rekavandi et al. [51] It is worth mentioning here that at pH < 4, metal ions start to leach from the perovskite phase, thereby limiting their use in acidic conditions [33]. On the other hand, perovskite oxides are stable in the pH range 6–8 and, therefore, can be successfully employed for wastewater treatment in this pH range [52].

3.4. *Effect of calcination temperature on catalytic degradation*

Fig. 6 shows the catalytic activity of the stoichiometric $SrFeO_3$ perovskites calcined at different temperatures for the degradation of methyl orange under dark conditions. The catalysts calcined at 200 °C and 400 °C showed no degradation activity. As discussed in section 3.1, the perovskite phase was not formed at these calcination conditions. This suggests that a crystalline $SrFeO_3$ phase is required for the catalytic degradation of methyl orange under dark reaction conditions. For the perovskite phase obtained at 600 °C, initially, a high (apparent) degradation rate was observed, resulting in a ~68 % decrease in the initial dye concentration after only 30 min. However, the degradation rate decreased with time, and the final C/C_0 was 0.08 at the end of the reaction, i.e., after 180 min. It is worth mentioning here that $SrCO_3$ present in the sample calcined at 600 °C was inactive for methyl orange degradation, see Fig. S4. The degradation activity of the catalysts calcined at different heating rates is plotted in Fig. S5, which shows that initially, the catalytic activity of both catalysts was almost similar, resulting in approximately 67 % degradation after 30 min. However, the final C/C_0 value obtained for the $SrFeO_3$ phase calcined at a heating rate of 2 °C/min was slightly lower than the $SrFeO_3$ obtained using a heating rate of 10 °C/min. The difference can be attributed to the difference in the surface areas of both catalysts, as summarized in Table 2. On the

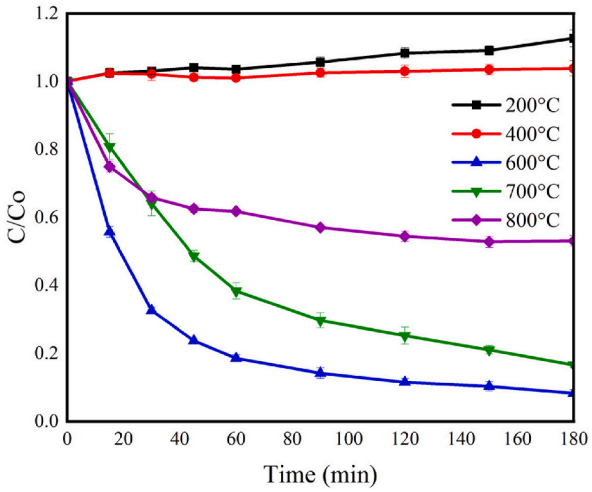

Fig. 6. Catalytic degradation of methyl orange as a function of time and calcination temperature of $SrFeO_3$. Reaction conditions: initial dye concentration (C_o) = 10 mgL^{-1}, catalyst amount = 500 mgL^{-1}, T = 60 °C in the dark. (For interpretation of the references to colour in this figure legend, the reader is referred to the Web version of this article.)

other hand, it can be observed from Fig. 6 that with an increase in the calcination temperature of $SrFeO_3$, both the (apparent) degradation rate and % degradation decreased. For example, for the catalyst prepared at 700 °C, the C/C_0 was 0.67 and 0.15 after 30 min and 180 min, respectively. Similarly, the C/C_0 value for $SrFeO_3$ calcined at 800 °C was 0.67 after 30 min, which slightly decreased to 0.54 after 180 min. To summarize, the overall % degradation decreased from 92 % to 47 % when the calcination temperature was increased from 600 °C to 800 °C, see Table 2. It is to be noted that the XRD patterns of these catalysts showed peaks only for the cubic $SrFeO_3$ phase. We speculate that the decrease in the surface area of the $SrFeO_3$ phase with increasing calcination temperature is mainly responsible for the decreasing activity trend observed in Fig. 6 [53]. Nonetheless, there can also be other reasons for the decreasing degradation activity, such as a change in the number of oxygen vacancies, crystallinity, etc.

3.5. O_2 dark activation by Sr-deficient $SrFeO_3$-based catalysts

As mentioned in the introduction, oxygen vacancies play an important role in the oxygen dark activation process. Oxygen vacancies can be introduced in the perovskite structure by metal doping, cation deficiency, or structural tilting [34,54–56]. In this work, we introduced cation deficiency at the A- and B-sites in the $SrFeO_3$ perovskite and evaluated its effect on the catalytic degradation of methyl orange in the dark. As seen from Table 2, the degradation efficiency of $SrFeO_3$ calcined at 600 °C is already high, reaching over 90 % in 180 min. As a result, any further enhancement in its catalytic activity would be limited and require changes in the reaction conditions to be apparent. On the other hand, the catalytic activity of stoichiometric $SrFeO_3$ calcined at 800 °C was only 46 % after 180 min. Therefore, we decided to calcine cation-deficient perovskites at 800 °C and compare their performance with stoichiometric $SrFeO_3$ prepared under the same conditions. We hypothesize that introducing cation deficiencies would compensate for the lower surface by creating active sites that improve catalytic activity. Fig. 7 shows the x-ray diffractograms of A-site deficient $Sr_{1-x}FeO_3$ catalysts (where $x = 0$, 0.05, 0.10, 0.15, and 0.20) calcined at 800 °C. A pure perovskite phase was obtained for $Sr_{1-x}FeO_3$ with $x = 0$, 0.05, and 0.10. However, we observed a shift in peak position towards higher angles for these oxides. This is probably due to a decrease in the cell volume of the $SrFeO_3$ lattice with increasing Sr deficiency at the A-site [57,58]. On the other hand, the peak positions of $Sr_{0.85}FeO_3$ and $Sr_{0.80}FeO_3$ corresponded to that of the stoichiometric $SrFeO_3$. Additionally, a left shoulder in the most prominent peak at ~32.2° and other small peaks at ~46.2° and ~57.8° confirmed the formation of a secondary $Sr_3Fe_2O_7$ phase. Based on these XRD patterns, we believe that $Sr_{1-x}FeO_3$ perovskites with $x > 0.10$ predominantly contained the stoichiometric $SrFeO_3$ phase. As reported in Table 3, the average crystallite size of all the $Sr_{1-x}FeO_3$ perovskites was smaller than the parent $SrFeO_3$ perovskite.

The scanning electron micrographs of the A-site deficient catalysts calcined at 800 °C are given in Fig. 8. A similar surface morphology of all the catalysts, comprising small particles fused because of high-temperature calcination, can be seen in Fig. 8. The combustion of organic matter during calcination resulted in significant voids between the interconnected particle networks. Analysis of SEM images using ImageJ software revealed that the average particle size of all Sr-deficient perovskites was smaller than $SrFeO_3$ and increased with non-stoichiometry. For example, the average particle size of $Sr_{0.95}FeO_3$ was around 150 nm ± 40 nm, three times smaller than the stoichiometric $SrFeO_3$ prepared and calcined under identical conditions. In the case of $Sr_{0.90}FeO_3$ and $Sr_{0.85}FeO_3$, the average particle size almost doubled at around 333 nm ± 94 nm. The particles in $Sr_{0.80}FeO_3$ had the highest aspect ratio with an average size of 378 nm ± 76 nm. Table 3 summarizes the BET surface area of A-site deficient perovskites. It can be noted that both $Sr_{0.95}FeO_3$ (16 m^2/g) and $Sr_{0.90}FeO_3$ (13 m^2/g) had a higher BET surface area than $SrFeO_3$ (10 m^2/g) under identical calcination conditions. On the other hand, the surface area of $Sr_{0.85}FeO_3$ (8 m^2/g) and $Sr_{0.80}FeO_3$ (9 m^2/g) was slightly lower than that of the stoichiometric oxide.

Fig. 9(a) compares the degradation activity of the A-site deficient $Sr_{1-x}FeO_3$ catalysts as a function of time, whereas Fig. 9(b) plots the final C/C_o value as a function of A-site non-stoichiometry. As discussed in section 3.4, the stoichiometric $SrFeO_3$ perovskite showed approximately 46 % degradation of methyl orange after 3 h. Lowering the amount of Sr at the A-site by 5 mol% increased the degradation of azo dye to approximately 79 %, albeit at a lower (apparent) rate. A further increase in Sr non-stoichiometry to 0.1 resulted in a C/C_0 of 0.06 for $Sr_{0.90}FeO_3$ after 3 h. When the Sr non-stoichiometry was increased to 15 % and 20 %, a significant reduction in the catalytic activity was observed. For example, $Sr_{0.85}FeO_3$ was able to catalytically remove only 72 % of the original methyl orange load, whereas this value further decreased to 44 % for $Sr_{0.80}FeO_3$. We speculate that for $S_{1-x}FeO_3$ perovskites with $x \leq 0.1$, the charge compensation mechanism leads to the generation of oxygen vacancies [59]. The oxygen vacancies and a higher surface area of these cation-deficient perovskites result in higher catalytic activity. The appearance of a secondary $Sr_3Fe_2O_7$ phase in $S_{1-x}FeO_3$ perovskites with $x = 0.15$ and 0.20 indicates that the crystal lattice can no longer support the cation deficiency by compensating charge. Because of this, the number of oxygen vacancies decreases in $S_{1-x}FeO_3$ perovskites with $x > 0.1$. A relatively lower surface area and oxygen vacancies cause the catalytic activity of A-site deficient $Sr_{1-x}FeO_3$ catalysts to decrease for $x > 0.1$. To summarize, the volcano-type activity trend observed here is due to the formation of oxygen vacancies at low Sr deficiency and the formation of a

Table 2
Effect of calcination on the % degradation of methyl orange at 60 °C in the dark.

Catalyst	Calcination temperature	% degradation after 30 min	% degradation after 180 min
$SrFeO_3$	200 °C	-	-
	400 °C	-	-
	600 °C	68	92
	700 °C	33	85
	800 °C	33	46

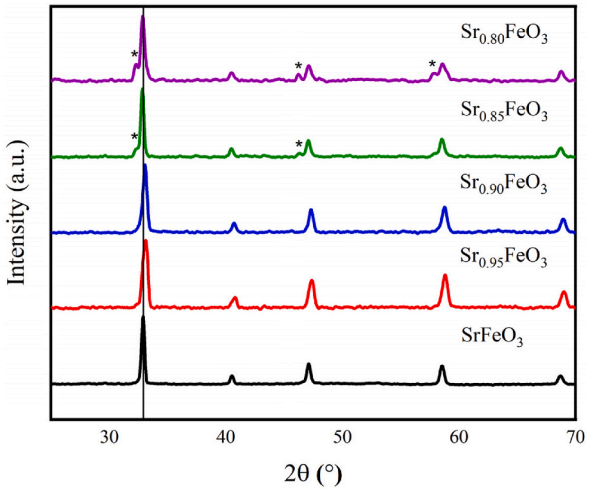

Fig. 7. X-ray diffractograms of A-site deficient $Sr_{1-x}FeO_3$ catalysts (where x = 0, 0.05, 0.10, 0.15, and 0.20) calcined at 800 °C for 3 h.

Table 3
Average crystallite size and BET surface area of A-site deficient $Sr_{1-x}FeO_3$ perovskites calcined at 800 °C for 3 h.

Catalyst	Calcination condition	Average crystallite size [nm]	BET Surface area [m^2/g]
$SrFeO_3$	800 °C	23	10
$Sr_{0.95}FeO_3$	800 °C	17	16
$Sr_{0.90}FeO_3$	800 °C	18	13
$Sr_{0.85}FeO_3$	800 °C	21	8
$Sr_{0.80}FeO_3$	800 °C	16	9

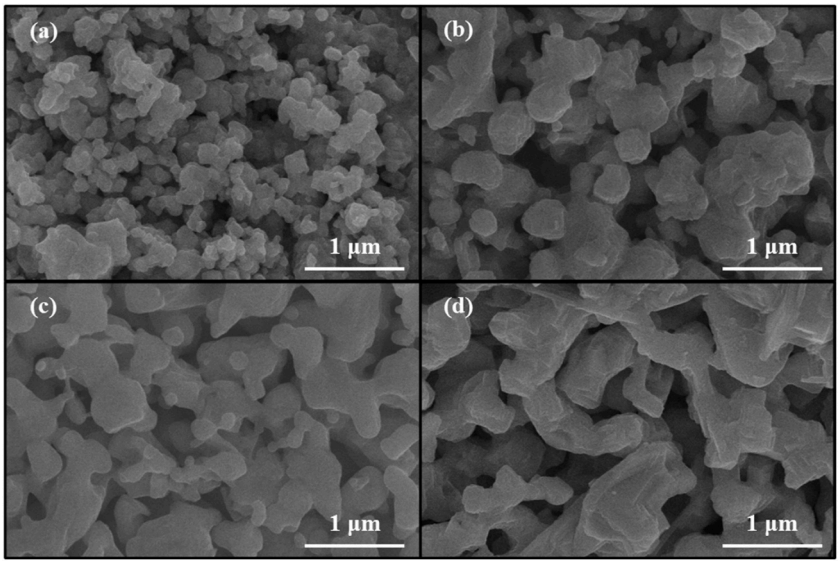

Fig. 8. Scanning electron micrographs of A-site deficient $SrFeO_3$: (a) $Sr_{0.95}FeO_3$, (b) $Sr_{0.90}FeO_3$, (c) $Sr_{0.85}FeO_3$, (d) $Sr_{0.80}FeO_3$.

stoichiometric $SrFeO_3$ phase at high Sr deficiency.

3.6. O_2 dark activation by Fe-deficient $SrFeO_3$-based catalysts

Next, we synthesized a series of $SrFe_{1-y}O_3$ perovskites in which the amount of Fe on the B-site was reduced in increments of 5 mol. % to 25 mol. %. Fig. 10 shows X-ray diffractograms of Fe-deficient $SrFe_{1-y}O_3$ catalysts, where y = 0, 0.05, 0.10, 0.15, 0.20, and 0.25, calcined at 800 °C for 3 h. Again, we did not observe any secondary phase or impurity in the diffraction patterns for $y \leq 0.10$, indicating

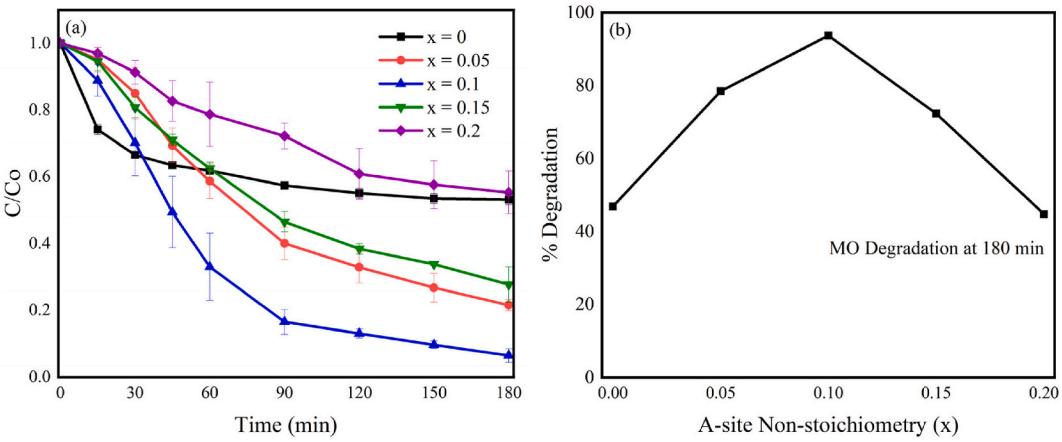

Fig. 9. (a) Effect of Sr-cation deficiency in $SrFeO_3$ on the degradation of methyl orange. Reaction conditions: $C_o = 10$ mgL^{-1}, catalyst amount = 500 mgL^{-1}, T = 60 °C, in the dark. (b) % degradation of methyl orange at 180 min as a function of A-site non-stoichiometry. (For interpretation of the references to colour in this figure legend, the reader is referred to the Web version of this article.)

that the $SrFeO_3$ perovskite can easily tolerate B-site cation deficiency up to y = 0.10 in the crystal lattice. Furthermore, we noticed a slight shift in the peak positions towards higher diffraction angles, which is most likely indicative of a decrease in the lattice volume of B-site deficient perovskites. When non-stoichiometry on the Fe-site was increased to 15 mol. %, a new peak appeared at ~32.3°, indicating the formation of a new phase in $SrFe_{0.85}O_3$. Moreover, it was observed that the peak positions of the B-site deficient perovskite phase moved slightly to lower diffraction angles. The x-ray diffractograms of $SrFe_{0.85}O_3$ and $SrFe_{0.80}O_3$ show three additional peaks at ~32.3°, ~42.0° and ~57.0°. These peaks were again matched with the $Sr_3Fe_2O_7$ phase [60], likely formed when excess SrO is excluded from the perovskite lattice. The XRD patterns in Fig. 10 indicate that a defect $SrFe_{1-y}O_3$ phase can only be obtained under the synthesis conditions employed here for $y \leq 0.15$. The average crystallite size of B-site non-stoichiometric perovskite oxides did not correlate with sample chemistry and was in the range 19–28 nm, as shown in Table 4.

The surface morphologies of Fe-deficient $SrFe_{1-y}O_3$ perovskites calcined at 800 °C were like that of A-site deficient $Sr_{1-x}FeO_3$ perovskites. It can be seen from Fig. S6 that all samples have granular surfaces comprising closely packed spherical particles. The large voids observed between the islands of particles were probably formed due to the combustion of organic matter during calcination. The average particle size of $SrFe_{0.95}O_3$ (458 nm ± 87 nm) was similar to that of $SrFeO_3$ (450 ± 121 nm). The average particle size decreased when Fe deficiency was further increased. For $SrFe_{0.90}O_3$, $SrFe_{0.85}O_3$, $SrFe_{0.80}O_3$, and $SrFe_{0.70}O_3$, the average size based on 30 particles was calculated to be 408 nm ± 69 nm, 355 nm ± 65 nm, 352 nm ± 91 nm, and 326 nm ± 70 nm, respectively. Table 4 shows that except for $SrFe_{0.90}O_3$, the BET surface areas of all Fe-deficient $SrFe_{1-y}O_3$ catalysts were low and in the range 5–8 m^2/g. On the other hand, the surface area of $SrFe_{0.90}O_3$ was measured to be 15 m^2/g.

Under dark conditions, the catalytic degradation of methyl orange by Fe-deficient $SrFeO_3$ oxides showed different behavior compared to Sr-deficient perovskite oxides. For example, both the $SrFeO_3$ and $SrFe_{0.95}O_3$ reduced the original dye concentration by ~46 % after 3 h. However, the observed rate of degradation was sluggish for $SrFe_{0.95}O_3$. This starkly differs from the catalytic activity of $Sr_{0.95}FeO_3$, which was 32 % higher than the stoichiometric perovskite. It can be noted from Tables 3 and 4 that the surface area of $Sr_{0.95}FeO_3$ is three times higher than that of $SrFe_{0.95}O_3$, which could be a reason for its higher degradation activity. Turning back to Fig. 11(a), we observed that lowering the amount of Fe on the B-site increased the (apparent) rate of degradation. Furthermore, the % degradation after 3 h for $SrFe_{0.90}O_3$, $SrFe_{0.85}O_3$, and $SrFe_{0.80}O_3$ was ~70 %, ~88 % and ~95 %, respectively. Table 4 shows that the surface area of these catalysts decreased in the order $SrFe_{0.90}O_3 > SrFe_{0.85}O_3 > SrFe_{0.80}O_3$. These results suggest that surface area alone cannot be used as a descriptor for the dye degradation activity of perovskite-based catalysts. We believe that an increase in the catalytic activity with A- or B-site deficiency in perovskites is linked with a combined effect of change in oxygen vacancies and surface area with composition. A detailed study is required to deconvolute the effect of non-stoichiometry and surface area on the degradation of azo dyes, which is beyond the scope of the present work. Finally, when we decreased the amount of Fe on the B-site to 30 mol.%, as in $SrFe_{0.70}O_3$, the catalytic activity decreased significantly, which is probably due to the formation of stoichiometric $SrFeO_3$ phase and the presence of a significant amount of $Sr_3Fe_2O_7$ phase, as evident from XRD patterns in Fig. 10.

4. Conclusion

Through this work, we have demonstrated that the structure of azo dyes significantly impacts their degradation in the dark *via* oxygen dark activation. A comparison of the degradation of four different azo dyes revealed that the presence of the electron-withdrawing groups in conjugation with the azo bond leads to an easier overall degradation of the azo dye. Furthermore, the position of these substituents also impacts the degradation kinetics due to their steric hindrance. Parametric studies revealed that an acidic pH favors the degradation of azo dyes. Turning toward the perovskite structure and composition, we found that introducing cation deficiency at A- or B-sites in $SrFeO_3$ enhanced the catalytic degradation of methyl orange. Degradation experiments showed a volcano-

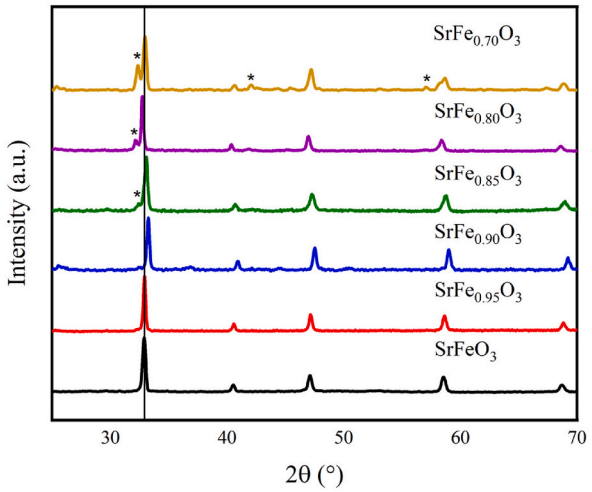

Fig. 10. X-ray diffractograms of B-site deficient $SrFe_{1-y}O_3$ catalysts (where y = 0, 0.05, 0.10, 0.15, 0.20 and 0.30) calcined at 800 °C for 3 h.

Table 4
Average crystallite size and BET surface area of B-site deficient $SrFe_{1-y}O_3$ perovskites calcined at 800 °C for 3 h.

Catalyst	Calcination condition	Average crystallite size [nm]	BET Surface area [m^2/g]
$SrFeO_3$	800 °C	23	10
$SrFe_{0.95}O_3$	800 °C	27	5
$SrFe_{0.90}O_3$	800 °C	27	15
$SrFe_{0.85}O_3$	800 °C	19	8
$SrFe_{0.80}O_3$	800 °C	28	7
$SrFe_{0.70}O_3$	800 °C	20	6

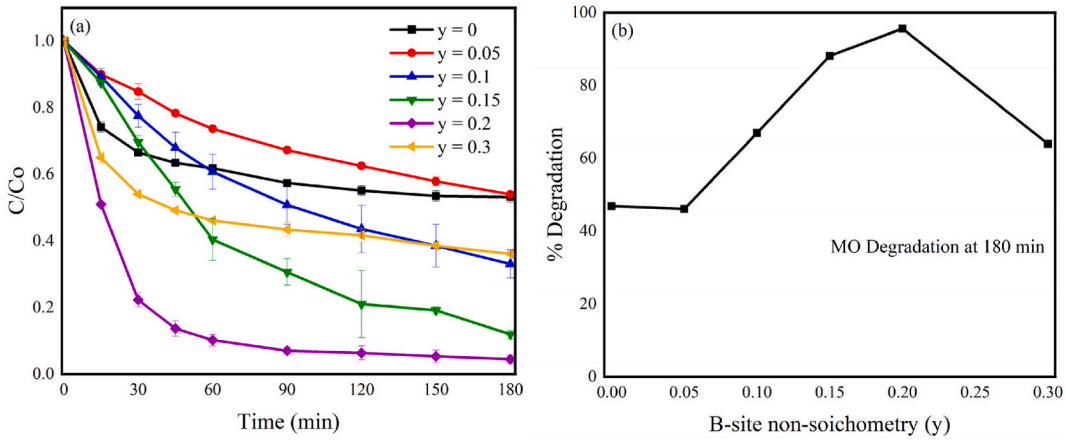

Fig. 11. (a) Effect of Fe-deficiency in $SrFeO_3$ on the degradation of methyl orange. Reaction conditions: C_o = 10 mgL^{-1}, catalyst amount = 500 mgL^{-1}, T = 60 °C, in the dark. (b) % degradation of methyl orange at 180 min as a function of B-site non-stoichiometry. (For interpretation of the references to colour in this figure legend, the reader is referred to the Web version of this article.)

type activity trend for Sr- and Fe-deficient $SrFeO_3$-based catalysts. We hypothesize that this is due to the formation of oxygen vacancies at low Sr/Fe deficiency and the formation of a stoichiometric $SrFeO_3$ phase at high Sr/Fe deficiency. Furthermore, the overall catalytic activity of nonstoichiometric perovskite oxides depends on the complicated interaction of oxygen non-stoichiometry and surface area. A detailed structural analysis of cation-deficient perovskite oxides is required to elucidate further the relation between cation deficiency and the degradation activity of perovskites.

CRediT authorship contribution statement

Sadia Manzoor: Investigation, Resources, Writing – original draft. **Qasim Imtiaz:** Writing – review & editing, Validation, Supervision, Methodology, Funding acquisition, Conceptualization.

Declaration of competing interest

The authors declare that they have no known competing financial interests or personal relationships that could have appeared to influence the work reported in this paper.

Appendix A. Supplementary data

Supplementary data to this article can be found online at https://doi.org/10.1016/j.heliyon.2024.e40157.

References

[1] A. Tkaczyk, et al., Synthetic organic dyes as contaminants of the aquatic environment and their implications for ecosystems: a review, Science of the total environment 717 (2020) 137222.
[2] Q. Zeng, et al., Biogenic sulfide for azo dye decolorization from textile dyeing wastewater, Chemosphere 283 (2021) 131158.
[3] C. Campalani, et al., Continuous flow photooxidative degradation of azo dyes with biomass-derived carbon dots, ChemPhotoChem 7 (5) (2023) e202200234.
[4] M.R. Samarghandi, et al., Degradation of azo dye Acid Red 14 (AR14) from aqueous solution using H2O2/nZVI and S2O82−/nZVI processes in the presence of UV irradiation, Water Environ. Res. 92 (8) (2020) 1173–1183.
[5] K. Golka, et al., Carcinogenicity of azo colorants: influence of solubility and bioavailability, Toxicology letters 151 (1) (2004) 203–210.
[6] H. Xue, et al., Efficient adsorption of anionic azo dyes on porous heterostructured MXene/biomass activated carbon composites: experiments, characterization, and theoretical analysis via advanced statistical physics models, Chem. Eng. J. 451 (2023) 138735.
[7] T. Kawakami, et al., Analysis of primary aromatic amines originated from azo dyes in commercial textile products in Japan, Journal of Environmental Science and Health Part A 45 (10) (2010) 1281–1295.
[8] R. Li, et al., Efficient decolorization of azo dye wastewater with polyaniline/graphene modified anode in microbial electrochemical systems, J. Hazard Mater. 421 (2022) 126740.
[9] Y. Yuan, et al., Intermittent electric field stimulated reduction-oxidation coupled process for enhanced azo dye biodegradation, Chem. Eng. J. 451 (2023) 138732.
[10] M. Shirzad-Siboni, et al., Removal of acid blue 113 and reactive black 5 dye from aqueous solutions by activated red mud, J. Ind. Eng. Chem. 20 (4) (2014) 1432–1437.
[11] R. Askari, et al., Synthesis of activated carbon from cherry tree waste and its application in removing cationic red 14 dye from aqueous environments, Appl. Water Sci. 13 (4) (2023) 90.
[12] A. Bes-Piá, et al., Study of the behaviour of different NF membranes for the reclamation of a secondary textile effluent in rinsing processes, J. Hazard Mater. 178 (1–3) (2010) 341–348.
[13] Y. Sun, et al., Synthesis and characterization of composite flocculant PAFS–CPAM for the treatment of textile dye wastewater, J. Appl. Polym. Sci. 131 (7) (2014).
[14] K. Treffry-Goatley, et al., Reverse osmosis treatment and reuse of textile dyehouse effluents, Desalination 47 (1–3) (1983) 313–320.
[15] L.R.S. Pinheiro, et al., Degradation of azo dyes: bacterial potential for bioremediation, Sustainability 14 (3) (2022) 1510.
[16] J. Mukherjee, et al., Advanced oxidation process for the treatment of industrial wastewater: a review on strategies, mechanisms, bottlenecks and prospects, Chemosphere (2023) 140473.
[17] K. Dutta, et al., Chemical oxidation of methylene blue using a Fenton-like reaction, J. Hazard Mater. 84 (1) (2001) 57–71.
[18] C.R. Holkar, et al., A critical review on textile wastewater treatments: possible approaches, J. Environ. Manag. 182 (2016) 351–366.
[19] A. Seidmohammadi, et al., A comparative study for the removal of methylene blue dye from aqueous solution by novel activated carbon based adsorbents, Progress in Color, Colorants and Coatings 12 (3) (2019) 133–144.
[20] D. Ma, et al., Critical review of advanced oxidation processes in organic wastewater treatment, Chemosphere 275 (2021) 130104.
[21] M. Sgroi, et al., Comparison of AOPs at pilot scale: energy costs for micro-pollutants oxidation, disinfection by-products formation and pathogens inactivation, Chemosphere 273 (2021) 128527.
[22] A. Lassoued, et al., Influence of iron content in Fe-based amorphous alloy catalysts on degradation of azo dyes by fenton-like process, J. Phys. Chem. Solid. 180 (2023) 111475.
[23] A. Riaza-Frutos, et al., Oxidation of an azo-dye via the photo-fenton process under heterogeneous and homogeneous conditions, Water 15 (9) (2023) 1787.
[24] Y. Wang, et al., Synergistic Ag/g–C3N4 H2O2 system for photocatalytic degradation of azo dyes, Molecules 29 (16) (2024) 3871.
[25] K. Wang, et al., Perovskite oxide catalysts for advanced oxidation reactions, Adv. Funct. Mater. 31 (30) (2021) 2102089.
[26] S.V. Besegatto, et al., Perovskite-based Ca-Ni-Fe oxides for azo pollutants fast abatement through dark catalysis, Appl. Catal. B Environ. 284 (2021) 119747.
[27] H. Chen, et al., Degradation of orange II dye under dark ambient conditions by MeSrCuO (Me= Mg and Ce) metal oxides, Separation and Purification Technology 205 (2018) 293–301.
[28] R. Vallavoju, et al., Degradation of organic pollutants in the presence of new Mn (II) complexes under ambient light or darkness conditions, J. Photochem. Photobiol. Chem. 442 (2023) 114775.
[29] J. Yang, et al., Oxygen vacancies and lewis acid sites synergistically promoted catalytic methane combustion over perovskite oxides, Environmental Science & Technology 55 (13) (2021) 9243–9254.
[30] M.Y. Leiw, et al., Dark ambient degradation of Bisphenol A and Acid Orange 8 as organic pollutants by perovskite SrFeO3− δ metal oxide, J. Hazard Mater. 260 (2013) 1–8.
[31] W. Wu, et al., Effective degradation of organic pollutants and reaction mechanism with flower-like AgBiO3/g-C3N4 composite, Colloids Surf. A Physicochem. Eng. Asp. 599 (2020) 124901.
[32] H. Chen, et al., Effective degradation of azo dyes in the dark by Cu2+ active sites in CaSrNiCu oxides, J. Environ. Chem. Eng. 6 (5) (2018) 5870–5878.
[33] M.L. Tummino, et al., Revisiting the catalytic activity of a doped SrFeO3 for water pollutants removal: effect of light and temperature, Appl. Catal. B Environ. 207 (2017) 174–181.
[34] J. Du, et al., Nonstoichiometric perovskite CaMnO3− δ for oxygen electrocatalysis with high activity, Inorganic chemistry 53 (17) (2014) 9106–9114.
[35] P. Liang, et al., Cation deficiency tuned LaCoO3− δ perovskite for peroxymonosulfate activation towards bisphenol A degradation, Chem. Eng. J. 409 (2021) 128196.

[36] S. PH Emmett Brunauer, E. Teller, The BET method, J. Am. Chem. Soc. 60 (1938) 309.
[37] K. Chu, et al., A general strategy to boost electrocatalytic nitrogen reduction on perovskite oxides via the oxygen vacancies derived from a-site deficiency, Adv. Energy Mater. 11 (11) (2021) 2003799.
[38] Y. Zhu, et al., An A-site-deficient perovskite offers high activity and stability for low-temperature solid-oxide fuel cells, ChemSusChem 6 (12) (2013) 2249–2254.
[39] F. Hao, et al., Sodium tungstate-promoted CaMnO3 as an effective, phase-transition redox catalyst for redox oxidative cracking of cyclohexane, J. Catal. 385 (2020) 213–223.
[40] A. Patterson, The Scherrer formula for X-ray particle size determination, Physical review 56 (10) (1939) 978.
[41] C. Schneider, W. Rasband, K. Eliceiri, NIH Image to ImageJ: 25 years of image analysis, Nat Methods 9 (2012) 671–675.
[42] M.B. Østergaard, et al., Kinetics of strontium carbonate formation on a Ce-doped SrFeO3 perovskite, Catalysts 12 (3) (2022) 265.
[43] E. Bagherisereshki, et al., Investigation into SrO/SrCO3 for high temperature thermochemical energy storage, Sol. Energy 160 (2018) 85–93.
[44] A. Majid, et al., The effect of preparation method and calcination temperature on the crystallite size and surface area of perovskite-type SrFeO x, J. Sol. Gel Sci. Technol. 32 (2004) 323–326.
[45] B. Kucharczyk, et al., The effect of the calcination temperature of LaFeO3 precursors on the properties and catalytic activity of perovskite in methane oxidation, Ceram. Int. 45 (2) (2019) 2779–2788.
[46] M.S. Goncalves, et al., Photochemical treatment of solutions of azo dyes containing TiO2, Chemosphere 39 (5) (1999) 781–786.
[47] C.-C. Hsueh, et al., Exploring effects of chemical structure on azo dye decolorization characteristics by Pseudomonas luteola, J. Hazard Mater. 154 (1–3) (2008) 703–710.
[48] M. Hou, et al., The effect of substituent groups on the reductive degradation of azo dyes by zerovalent iron, J. Hazard Mater. 145 (1–2) (2007) 305–314.
[49] W. Tang, et al., TiO2/UV photodegradation of azo dyes in aqueous solutions, Environmental technology 18 (1) (1997) 1–12.
[50] D. Chen, et al., Photodegradation kinetics of 4-nitrophenol in TiO2 suspension, Water Res. 32 (11) (1998) 3223–3234.
[51] N. Rekavandi, et al., Methyl orange degradation over nano-LaMnO3 as a green catalyst under the mild conditions, Nanochemistry Research 4 (1) (2019) 1–10.
[52] D. Palma, et al., Main issues in the synthesis and testing of thermocatalytic Ce-doped SrFeO3 perovskites for wastewater pollutant removal, Inorganics 11 (2) (2023) 85.
[53] S. Diodati, et al., Highly crystalline strontium ferrites SrFeO 3− δ: an easy and effective wet-chemistry synthesis, Dalton Trans. 41 (18) (2012) 5517–5525.
[54] F. Yang, et al., Defect chemistry and electrical properties of sodium bismuth titanate perovskite, J. Mater. Chem. A 6 (13) (2018) 5243–5254.
[55] W. Sun, et al., Oxygen vacancy mediated La1-xCexFeO3-δ perovskite oxides as efficient catalysts for CWAO of acrylic acid by A-site Ce doping, Appl. Catal. B Environ. 245 (2019) 20–28.
[56] J. Hwang, et al., Tuning perovskite oxides by strain: electronic structure, properties, and functions in (electro) catalysis and ferroelectricity, Mater. Today 31 (2019) 100–118.
[57] Y. Zhu, et al., Enhancing electrocatalytic activity of perovskite oxides by tuning cation deficiency for oxygen reduction and evolution reactions, Chem. Mater. 28 (6) (2016) 1691–1697.
[58] S. Li, et al., Non-stoichiometry, structure and properties of proton-conducting perovskite oxides, Solid State Ionics 361 (2021) 115571.
[59] G.C. Kostogloudis, et al., Properties of A-site-deficient La0. 6Sr0. 4Co0. 2Fe0. 8O3− δ-based perovskite oxides, Solid State Ionics 126 (1–2) (1999) 143–151.
[60] S. Gabra, et al., The use of strontium ferrite perovskite as an oxygen carrier in the chemical looping epoxidation of ethylene, Appl. Catal. B Environ. 286 (2021) 119821.